BIOCHEMISTRY
including biophysical chemistry & molecular biology
Article

Biochemistry **2010,** *49,* 6973–6983 6973
DOI: 10.1021/bi100647z

Evidence That Histidine Protonation of Receptor-Bound Anthrax Protective Antigen Is a Trigger for Pore Formation†

D. Shyamali Wimalasena,‡ Blythe E. Janowiak,§ Scott Lovell,∥ Masaru Miyagi,⊥ Jianjun Sun,§,○ Haiying Zhou,‡,◇ Jan Hajduch,# Chaya Pooput,# Kenneth L. Kirk,# Kevin P. Battaile,△ and James G. Bann*,‡

‡*Department of Chemistry, Wichita State University, Wichita, Kansas 67260,* §*Department of Microbiology and Molecular Genetics, Harvard Medical School, Boston, Massachusetts 02115,* ∥*Del Shankel Structural Biology Center, The University of Kansas, Lawrence, Kansas 66047,* ⊥*Case Center for Proteomics and Bioinformatics, Department of Pharmacology, Department of Ophthalmology and Visual Sciences, Case Western Reserve University, 10900 Euclid Avenue, Cleveland, Ohio 44106-4988,* #*Laboratory of Bioorganic Chemistry, National Institute of Diabetes and Digestive and Kidney Diseases, National Institutes of Health, Bethesda, Maryland 20892-0810, and* △*IMCA-CAT, Advanced Photon Source, Argonne National Laboratory, 9700 South Cass Avenue, Building 435A, Argonne, Illinois 60439.* ○*Current address: Department of Biological Sciences, University of Texas at El Paso, El Paso, Texas 79968-0519.* ◇*Current address: Department of Chemistry, University of Missouri—Columbia, 125 Chemistry Building, 601 S. College Ave., Columbia, MO 65211-7600.*

Received April 27, 2010; Revised Manuscript Received July 16, 2010

ABSTRACT: The protective antigen (PA) component of the anthrax toxin forms pores within the low pH environment of host endosomes through mechanisms that are poorly understood. It has been proposed that pore formation is dependent on histidine protonation. In previous work, we biosynthetically incorporated 2-fluorohistidine (2-FHis), an isosteric analogue of histidine with a significantly reduced pK_a (∼1), into PA and showed that the pH-dependent conversion from the soluble prepore to a pore was unchanged. However, we also observed that 2-FHisPA was nonfunctional in the ability to mediate cytotoxicity of CHO-K1 cells by LF_N−DTA and was defective in translocation through planar lipid bilayers. Here, we show that the defect in cytotoxicity is due to both a defect in translocation and, when bound to the host cellular receptor, an inability to undergo low pH-induced pore formation. Combining X-ray crystallography with hydrogen−deuterium (H−D) exchange mass spectrometry, our studies lead to a model in which hydrogen bonds to the histidine ring are strengthened by receptor binding. The combination of both fluorination and receptor binding is sufficient to block low pH-induced pore formation.

Anthrax toxin is an AB toxin secreted by *Bacillus anthracis* and is required for disease pathogenesis (*1*). The B component, the protective antigen (PA),[1] is an 83 kDa, four domain protein that binds to the extracellular von Willebrand factor A (vWA) integrin-like I domain of either one of two identified host cell receptors, anthrax toxin receptor 1/tumor endothelial marker 8 (ANTXR1/TEM8) or anthrax toxin receptor 2/capillary morphogenesis protein 2 (ANTXR2/CMG2) (*2*, *3*). Binding of PA to the receptor vWA domain is followed by cleavage of PA into two fragments of 63 and 20 kDa, by a cell-surface furin protease (*4*), leading to the spontaneous formation of a ring-shaped heptameric $(PA_{63})_7$ structure termed the prepore (*5*). Formation of the prepore creates binding sites for the enzymatic A components, edema factor (EF) and lethal factor (LF), which bind with a stoichiometry of three EF or LF's per prepore (*6*). In addition, PA has been shown recently to form functional octameric $(PA_{63})_8$ complexes on host cell surfaces (∼20−30% of the population of oligomers), which are capable of binding four EF or LF's per octamer (*7*).

Next, the entire complex is endocytosed (*8*, *9*) and trafficked to late endosomes which become acidic (*10*). At the low pH of the endosome (∼5−6), the prepore undergoes a major conformational change in which β-strands from domain 2 unfold and insert into the endosomal membrane, forming a transmembrane β-barrel structure called the pore (*11*−*14*). Formation of the pore allows EF or LF, in an unfolded state, to translocate through the pore into the cell cytosol, a process that is driven by the established pH gradient between the endosome and cytosol (*15*, *16*). Once in the cytosol, EF and LF are able to

†This work supported by NIH 5P20 RR17708 (J.G.B. and S.L.), NIH R01 AI022021 to R. John Collier (financial support to B.E.J. and J.S.), NIH 1F32 AI077280 (B.E.J.), Cleveland Foundation (M.M.), and intramural research funds from the NIDDK, NIH (K.L.K.). Use of the IMCA-CAT beamline 17-BM at the Advanced Photon Source was supported by the companies of the Industrial Macromolecular Crystallography Association through a contract with the Center for Advanced Radiation Sources at the University of Chicago. Use of the Advanced Photon Source was supported by the U.S. Department of Energy, Office of Science, Office of Basic Energy Sciences, under Contract W-31-109-Eng-38.

*To whom correspondence should be addressed. Tel: (316) 978-7373. Fax: (316) 978-3431. E-mail: Jim.Bann@wichita.edu.

[1]Abbreviations: ANTXR1, anthrax toxin receptor 1; ANTXR2, anthrax toxin receptor 2; C−F, carbon−fluorine bond; CHO-K1, Chinese hamster ovary K1 cells; CMG2, capillary morphogenesis protein 2; EF, edema factor; 2-FHis, 2-fluorohistidine; 2-FHisPA, the 83 kDa form of 2-FHis-labeled PA; $(2\text{-FHisPA}_{63})_7$, the 63 kDa, heptameric form of 2-FHis-labeled PA; H−D, hydrogen−deuterium; Gdn, guanidinium; HSQC, heteronuclear single-quantum coherence; LC, liquid chromatography; LF, lethal factor; LF_N, N-terminal PA binding domain of LF; LF_N−DTA, N-terminal PA binding domain−diphtheria toxin A domain fusion protein; MS, mass spectrometry; MTS-ET, 2-(trimethylammoniumethylmethanethiosulfonate; PA, protective antigen; SDS−PAGE, sodium dodecyl sulfate−polyacrylamide gel electrophoresis; SMRC, strongest methyl resonance carbon-13; TEM8, tumor endothelial marker 8; vWA, von Willebrand factor A domain; WT, wild type.

Published on Web 07/22/2010

manifest their toxic effects: EF is an adenylate cyclase (*17*) and LF is a zinc-dependent metalloprotease (*18*).

Although we have significantly advanced our understanding of PA and the mechanisms related to translocation (*19*, *20*), it is not yet known specifically which amino acid residues are responsible for triggering pore formation in response to low pH. Originally, histidine protonation was proposed as a likely mechanism for pore formation, since the pH at which pore formation occurs in solution (~pH 7) is near the pK_a of histidine (~6) (*21*, *22*). In addition, four of the ten histidines in PA (nine in the prepore) reside within a sequence of domain 2 that comprises the β-barrel portion of the pore (His 299, His 304, His 310, and His 336) (*13*, *14*).

In previous work, we have shown that uniform labeling of PA with 2-fluorohistidine (2-FHis), an isosteric analogue of histidine having a reduced side-chain pK_a (~1), has differential effects on the 83 kDa 2-FHisPA and prepore (2-FHisPA$_{63}$)$_7$ structures (*23*). While 2-FHisPA exhibits greater stability to pH (pK_{app} of 3.6 vs 5.9 for WT PA), the 2-FHis-prepore can undergo the conformational change to a pore at pH values similar to those of the WT prepore. Because of the reduced pK_a of 2-FHis which likely prevents protonation at low pH (~5), we took this as evidence that histidine protonation is not the trigger for pore formation. However, aside from the effect on pore formation, we also observed little to no translocation of the N-terminal domain of lethal factor (LF_N) through the pore of the (2-FHisPA$_{63}$)$_7$, as measured by ion conductance through planar lipid bilayers. Additionally, 2-FHisPA was found to be ineffective in mediating cytotoxicity of CHO-K1 cells by LF_N−DTA, a fusion between LF_N, the N-terminal prepore binding domain of lethal factor, and the catalytic A-domain of diphtheria toxin.

Here, we further examine the origin of the defect in cytotoxicity. We show that the defect cannot be explained solely through a defect in translocation and show that pore formation of the receptor-bound 2-FHis-prepore is blocked. Our combined results lead to a model in which binding to the cellular receptor enhances hydrogen-bonding interactions to the histidines, which prevents premature protonation and pH unfolding to form a membrane spanning pore until it reaches the correct cellular compartment.

EXPERIMENTAL PROCEDURES

Mutagenesis, Production, and Purification. *Escherichia coli* strain UTH780, a strain auxotrophic for histidine, was used for labeling PA and mutant proteins with 2-FHis (*24*). Synthesis of 2-FHis was carried out as described previously (*25*). Expression, production, and purification of PA, and labeling with 2-FHis, were carried out as described previously (*23*). Proteins labeled with 2-FHis were greater than 95% labeled as determined by mass spectrometry (*23*). Mutagenesis was carried out using the QuikChange mutagenesis kit (Stratagene, La Jolla, CA) and the plasmid pQE80-PA, with oligonucleotide primers obtained from Sigma Genosys. Sequences were verified by the Protein and Nucleic Acid Chemistry Laboratory at Washington University in St. Louis (St. Louis, MO). The vWA domain of CMG2, encoding residues 38−218, was produced as a GST fusion from plasmid pGEX-4T1-CMG2$^{38-218}$, using *E. coli* strain BL-21 as described previously (*26*, *38*).

Cytotoxicity Assay. The ability of WT, 2-FHis labeled, and mutant PA proteins to mediate cytotoxicity of CHO-K1 cells by LF_N−DTA was carried out as described previously (*23*). Briefly, CHO-K1 cells were incubated in HAM F-12 medium with 100 nM LF_N−DTA and various concentrations of either WT or 2-FHisPA for 4 h at 37 °C in 96-well microtiter plates. The medium was removed, and new Leu-free medium was added which was supplemented with [^{3}H]leucine (172 Ci/mmol, 5.8 nM final concentration of leucine). After incubating the cells for 1 h, the cells were washed with phosphate-buffered saline, and the amount of incorporation of [^{3}H]leucine from the total cells was measured as described (*27*, *28*).

Translocation in Planar Lipid Bilayers. Translocation experiments in black lipid membranes were carried out using a planar lipid workstation (Warner Instruments, Hamden, CT). Lipid membranes were comprised of 3% 1,2-diphantanoyl-*sn*-glycero-3-phosphocholine (DPhPC) in *n*-decane (Avanti Polar Lipids, Alabaster, AL). Typically, 0.1 μL of a 3.1 mg/mL solution of (PA$_{63}$)$_7$ was added to the cis membrane which was held at pH 5.5. LF_N or LF_N−DTA (10 nM) was added to the *cis* compartment, and the blockage in channel conductance was measured (*19*). Translocation was initiated by the addition of KOH to the trans side of the membrane to pH 7.2. Data were analyzed using Axograph and reported as fraction of LF_N or LF_N−DTA translocated.

Potassium Release Assay. Measurement of the kinetics of potassium release from purified 1,2-dioleoyl-*sn*-glycero-3-phosphocholine (DOPC) vesicles was done as described previously (*23*, *29*).

SMRC NMR. SMRC experiments were performed in a manner similar to that described by Rajapaksha (*26*). CMG2 was labeled uniformly with ^{13}C using M9 minimal media in which the glucose was replaced with [U-^{13}C]glucose (0.2%), using BL21-DE3 cells transformed with the pGEX-4T1 CMG2$^{38-218}$ gene and purifying as described previously (*26*).

Deuteration, Digestion, and Mass Spectrometry of PA and the PA−CMG2 Complex. PA (1 nmol) and the PA−CMG2 complex (1 nmol of PA and 5 nmol of CMG2) were incubated in 200 μL of 50 mM CHES buffer (pH* 9.5) made with D_2O that contains 50 mM NaCl and 1 mM $MgCl_2$ at 37 °C for 48 h. The pH* value is the direct pH meter reading of the D_2O buffer solutions uncorrected for the isotope effect at the glass electrode. The final D_2O content in the reaction mixture was 95%. The reaction was stopped by mixing with 5 μL of formic acid, and the protein was freed from the buffer salts using an Ultra Micro Spin C4 column (Nest Group, Southboro, MA) according to the manufacturer's instructions and dried in a Speed Vac. An aliquot (250 pmol) was dissolved in 50 mM ammonium bicarbonate and digested either with a combination of trypsin (0.25 μg) and chymotrypsin (0.25 μg) or with chymotrypsin alone (0.25 μg) at room temperature for 30 min. The proteases used were immobilized proteases from Princeton Separations (Adelphia, NJ). All of the rapidly exchanging deuterons such as the backbone amide deuterons are back-exchanged for hydrogens during the digestion.

The digests were analyzed by LC-MS/MS using an UltiMate 3000 LC system (Dionex, San Francisco, CA) interfaced to a LTQ-FT mass spectrometer (Thermo-Finnigan, Breman, Germany). The protein digests (10 pmol) were injected into a reversed-phase C18 PepMap trapping column (0.3 × 5 mm, 5 μm particle size; Dionex) equilibrated with 0.1% formic acid/2% acetonitrile (v/v) and washed for 5 min with the equilibration solvent at a flow rate of 25 μL/min, using an isocratic loading pump operated through an autosampler. After the washing step, the trapping column was switched in-line with a reversed-phase C18 Acclaim PepMap 100 column (0.075 × 150 mm; Dionex), and the peptides were

chromatographed using a linear gradient of acetonitrile from 2% to 50% in aqueous 0.1% formic acid over a period of 60 min at 300 nL/min, and the eluate was directly introduced into the mass spectrometer. The mass spectrometer was operated in a data-dependent MS to MS/MS switching mode, with the two most intense ions in each MS scan subjected to MS/MS analysis. The full MS scan was performed at a resolution of 60000, and the subsequent MS/MS analysis was performed at a resolution of 30000. The total scan cycle frequency was approximately 1 s. The precursor ion isolation width was set to be $m/z \pm 2.0$ that allowed the transmission of the M and M + 2 isotopic ions of the peptide for CID. The data were entirely collected in the profile mode. Xcalibur software (version 2.0.5, build 0704; Thermo-Finnigan) was used for instrument control, data acquisition, and data processing.

The pseudo-first-order rate constant (k_φ) of the H−D exchange reaction was determined by monitoring the changes in the ratios of M + 1/M isotopic peak of a given peptide before and after the H−D exchange reaction, $I_{M+1}(0)/I_M(0)$ and $I_{M+1}(t)/I_M(t)$, respectively, using the equation:

$$k_\varphi = -\ln\left\{1 - \left[\frac{(R(t) - R(0))}{1 + R(t) - R(0)}\right]\frac{1}{P}\right\}\Big/ t$$

where $R(0) = I_{M+1}(0)/I_M(0)$ and $R(t) = I_{M+1}(t)/I_M(t)$, P is the fractional D_2O content in the solvent ($P = 1$ when D_2O content is 100%), and t is the incubation time (hours). The half-lives ($t_{1/2}$, day) of the exchange reaction were estimated using the equation: $t_{1/2}(\text{day}) = \ln 2/k_\varphi/24$.

X-ray Crystallography. 2-FHisPA concentrated to 16.5 mg/mL in 150 mM NaCl and 10 mM Tris, pH 8.0, was screened for crystallization in Compact Jr. (Emerald BioSystems) sitting drop vapor diffusion plates. Crystals were grown using 0.5 μL of crystallization solution (30% PEG 400, 100 mM Tris, pH 8.2) and 0.5 μL of protein equilibrated against 100 μL of crystallization solution at 20 °C. Elongated prismatic crystals were obtained within 24 h. Single crystals were transferred to a fresh drop of crystallization solution and frozen in liquid nitrogen for data collection. Data were collected at the Advanced Photon Source IMCA-CAT beamline 17BM using an ADSC Quantum 210r CCD detector. Intensities were integrated and scaled using the HKL2000 package (*30*). The coordinates from a previous structure of 2-FHisPA, determined in-house, were used for initial refinement against the processed diffraction data. Positional and isotropic *B*-factor refinement was conducted with Refmac (*31*). Anisotropic displacement parameters were modeled in the final stages of refinement by including four TLS groups as determined from the TLSMD server (*32*). Manual model building was performed with Coot (*33*). Side-chain residues that were not masked by electron density were truncated to the point where electron density was present. Positive difference ($F_o - F_c$) electron density consistent with a PEG 400 molecule was observed at a 3σ contour level near Lys 496 and was subsequently modeled at this site. Structure validation was carried out using Molprobity (*34*). The coordinates and structure factors have been deposited to the Protein Data Bank with the accession code 3MHZ.

RESULTS

Identification of H299 as the Cause of the Defect in Translocation upon Labeling with 2-FHis. Toward understanding the observed defect in translocation associated with 2-FHis labeling, we reasoned that replacing the His residues lining the PA pore channel with 2-FHis might alter the structure of the lumen of the pore and block translocation or, alternatively, that histidine protonation is critical to the mechanism of protein translocation. Biochemical experiments using cysteine-scanning mutagenesis combined with 2-(trimethylammonium)ethyl-methanethiosulfonate (MTS-ET) labeling have demonstrated that H304 and H310 are the only two histidine residues within the lumen of the channel, while H299 and H336 lie on the exterior facing the lipid bilayer (*13*, *14*). In the course of our studies, we constructed a double mutant of H304/310Q and an H299Q mutant to probe the role of these histidines in translocation. These mutants were able to insert into membranes and translocate LF_N as measured by ion conductance across planar lipid bilayers, with kinetics similar to those of WT PA (Figure 1A). These mutants were then uniformly labeled with 2-FHis and purified, and the translocation experiments were repeated. While translocation was blocked for the 2-FHisPA and the 2-FH304/310Q mutant, the 2-FH299Q mutant was able to translocate LF_N (Figure 1A), suggesting that fluorination of H299 causes the defect in LF_N translocation.

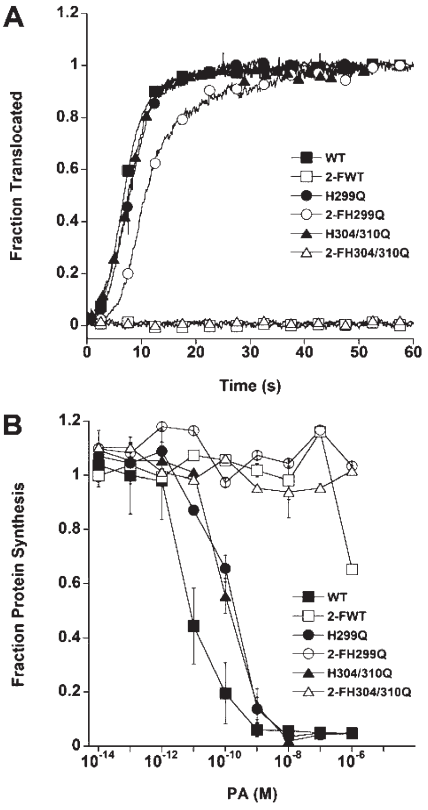

FIGURE 1: (A) Translocation of LF_N shown as a function of time during macroscopic conductance measurements taken using a planar phospholipid bilayer system. Representative planar lipid bilayer macroscopic conductance records (from experiments of $n \geq 3$) are shown for labeled (open symbols: □, 2-FWT; ○, 2-FH299Q; △, 2-FH304/310Q) and unlabeled (closed symbols: ■, WT; ●, H299Q; ▲, H304/310Q) WT PA and histidine mutant PA proteins as indicated. Records are normalized as fraction translocated. (B) Cytotoxicity as determined by protein synthesis inhibition mediated by PA proteins translocating LF_N−DTA into the cytosol of CHO-K1 cells. Plotted are the mean of ≥three experiments plus the standard deviation. Cytotoxicities of unlabeled WT and histidine mutant PA proteins (closed symbols: ■, WT; ●, H299Q; ▲, H304/310Q) and 2-FHis-labeled WT and histidine mutant PA proteins (open symbols: □, 2-FWT; ○, 2-FH299Q; △, 2-FH304/310Q) are shown.

H299Q PA Labeled with 2-FHis Does Not Restore the Defect in Cytotoxicity. Despite the ability to translocate LF_N, the 2-FH299Q mutant was unable to restore the defect in cytotoxicity (Figure 1B). Along with the unlabeled WT, H299Q and H304/310Q mutants, which are functional and cytotoxic, we have included the corresponding WT and mutants labeled with 2-FHis. The 2-FHis-labeled proteins were all noncytotoxic. Since the planar bilayer experiments utilize LF_N, whereas the CHO-K1 cell experiments utilize LF_N−DTA, we hypothesized that perhaps the inability of the 2-FH299Q mutant to mediate cytotoxicity was related to an inability to translocate LF_N−DTA, which is a significantly longer substrate than LF_N and may therefore be more energetically difficult to unfold and move through the membrane. Experiments in which LF_N−DTA was used in the translocation assay indicated that both the H299Q- and the 2-FH299Q-labeled proteins were able to translocate LF_N−DTA (Figure S1, Supporting Information), suggesting that other mechanisms may be responsible for the defect in cytotoxicity and must not be limited to translocation.

Effect of 2-FHis Labeling on Pore Formation in the Presence of the Receptor. In our previous study we showed that both WT and 2-FHisPA proteins were able to bind to the cell surface, indicating that interactions with the host cellular receptor were unperturbed (*23*). However, it was possible that effects on steps subsequent to receptor binding, along the pathway leading up to translocation, may contribute to the observed defect in cytotoxicity. Receptor binding decreases the pH required to initiate pore formation by ~1−2 pH units, from a pH of ~7 to ~5−6 (*35*−*37*). We therefore purified the receptor binding vWA domain of CMG2 to study the effect of the receptor on low pH-induced pore formation.

PA has been shown to bind the vWA domain of CMG2 with high affinity (~200 pM) (*38*). Both PA and 2-FHisPA could form a stable complex with the vWA domain of CMG2 as determined by a gel shift assay (Figure 2A) (*26*). In our previous study we showed that both the WT and 2-FHis prepore proteins exhibited similar pH-dependent properties in terms of pore formation, as determined by SDS−PAGE as well as by monitoring kinetics of potassium release from purified liposomes (*23*). In the current study, we also monitored pore formation using similar assays, but in the presence of the vWA domain. Using the SDS−PAGE assay, while pore formation of WT $(PA_{63})_7$ could be observed at pH 6, pores of $(2\text{-FHisPA}_{63})_7$ were only faintly observed at pH 6 and 5, suggesting that pore formation of $(2\text{-FHisPA}_{63})_7$, in the presence of the vWA domain, is largely blocked (Figure 2B). Likewise, potassium release experiments showed that while the WT $(PA_{63})_7$ exhibits the expected increase in potassium release in the presence of the vWA domain (*29*), potassium release of $(2\text{-FHisPA}_{63})_7$ was ~10% of that of the WT−vWA domain complex (Figure 2C). This indicates that the vWA domain of the receptor, when bound to $(2\text{-FHisPA}_{63})_7$, causes a change in the $(2\text{-FHisPA}_{63})_7$ prepore state such that it is largely incapable of forming a pore.

Block in Receptor Dissociation from the 2-FHis-Labeled Prepore at Low pH. Rainey and co-workers have demonstrated that receptor dissociation occurs at pH values commensurate with pore formation, and thus it was possible that the block in pore formation may be a consequence of an inability of the receptor to dissociate from the $(2\text{-FHisPA}_{63})_7$ prepore. To provide evidence of receptor dissociation from the $(2\text{-FHisPA}_{63})_7$ prepore, we followed the pH dependence of the 1-D ^1H−^{13}C-HSQC NMR spectrum of a uniformly ^{13}C-labeled vWA

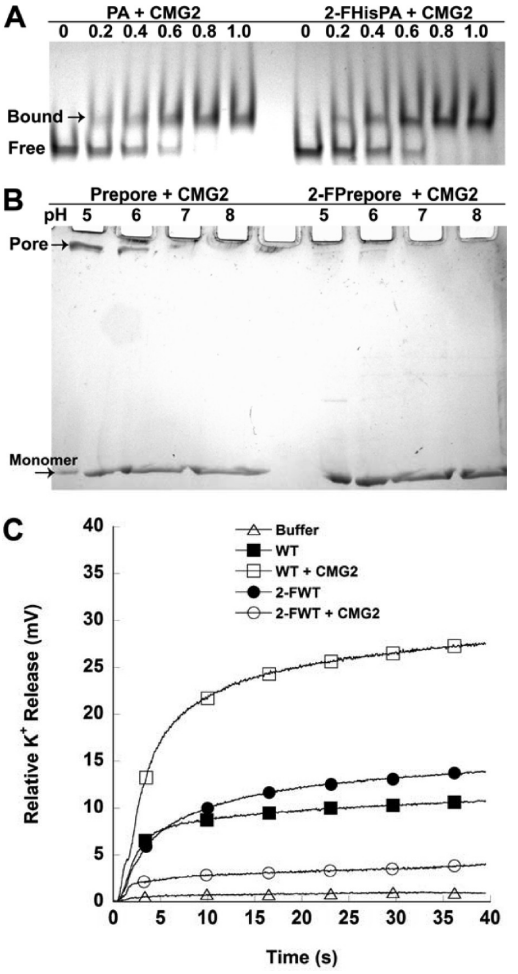

FIGURE 2: (A) Binding of CMG2 to WT PA (left lanes) and 2-FHisPA (right lanes). Each lane contains 5 μM PA; the numbers above each lane correspond to the stoichiometry of CMG2 to PA. Samples were loaded onto a native 4−20% PAGE gel and run for ~3 h at constant voltage (40 mV). (B) Conversion of $(PA_{63})_7$ and $(2\text{-FHisPA}_{63})_7$ from a prepore (pH 8.5) to a pore state in the presence of CMG2. Each lane contains ~0.9 μM PA_{63} and 5 μM CMG2. Buffers (350 mM final) used were BisTris (pH 5 and 6) and HEPES (pH 7 and 8). (C) Potassium release from purified liposomes. Liposomes contained 150 mM KCl and 10 mM HEPES (pH 7.4) and were bathed in 50 mM sodium acetate and 150 mM NaCl (pH 5.0). PA prepore (3 nM), either alone (■, WT; ●, 2-FHisPA) or complexed with CMG2 (40 nM) (□, WT; ○, 2-FHisPA), was added to the liposome solution, and K^+ release was monitored with a K^+-selective electrode (Orion Research) continuously. Buffer control is shown (△). The traces shown are representative of three experiments.

domain of CMG2 in the presence of either $(2\text{-FHisPA}_{63})_7$ or WT $(PA_{63})_7$ by focusing on the strongest methyl resonance of carbon-13 (SMRC) (Figure 3) (*26*, *39*). In this assay, we used an approximate 2-fold higher concentration of ^{13}C-CMG2 in order to observe residual ^1H resonance intensity, since a 1:1 stoichiometry results in extreme line broadening and a complete loss in resonance intensity. The results at pH 8.1 show that both the WT and 2-FHis-labeled prepore proteins are able to associate with ^{13}C-CMG2, as shown by a significant decrease in resonance intensity (compare intensity with no prepore added (spectrum A) to that with prepore proteins added (spectra B and C)). At a reduced pH of 5.7, where pore formation is known to occur, resonance intensity of ^{13}C-CMG2 bound to the WT $(PA_{63})_7$ prepore increased, indicative of receptor release, while the intensity of ^{13}C-CMG2

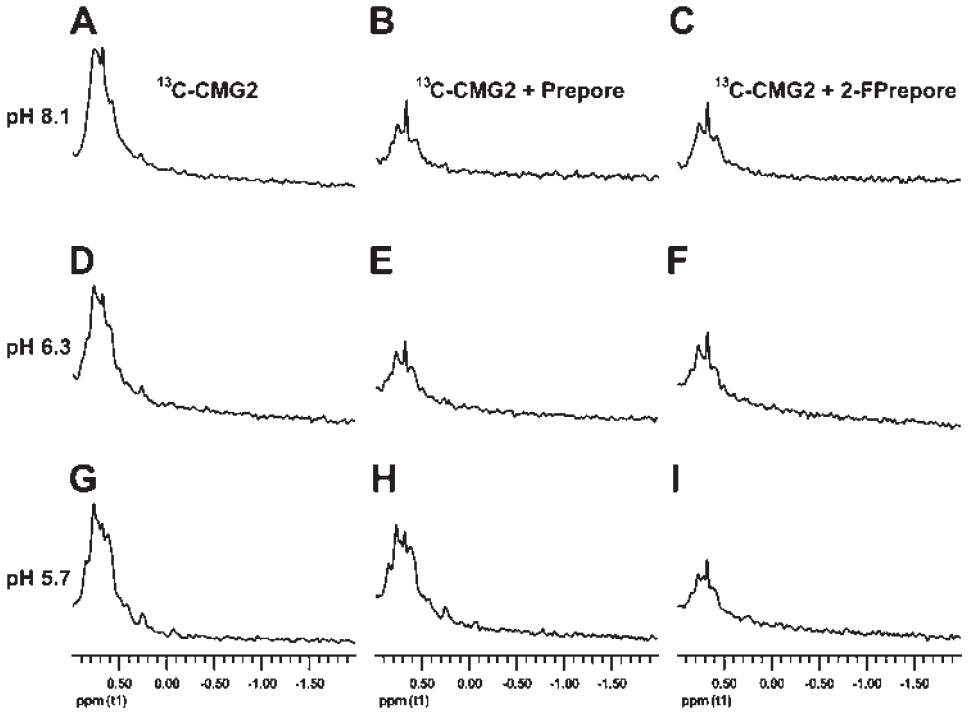

FIGURE 3: $^{1}H-^{13}C$-HSQC to determine the influence of pH on release of ^{13}C-CMG2 from the prepore of $(PA_{63})_7$ and $(2\text{-}FHisPA_{63})_7$. All experiments were performed at 25 °C. Either PA_{63} (31 μM) or $2\text{-}FHisPA_{63}$ (39 μM) in 0.5 M NaCl and 20 mM Tris-d_{11}, pH 8.5, was added to ^{13}C-labeled CMG2 (20 μL) in 0.1 M NaCl and 10 mM HEPES-d_{18}, pH 7.4, in a volume of 100 μL to give a final concentration of 15 μM PA_{63} and $2\text{-}FHisPA_{63}$ and 30 μM CMG2. The binding reaction was incubated for ~1 h at room temperature, to which 400 μL of a universal pH buffer (56 mM each of cacodylic acid-d_7, BisTris-d_{19}, and Tris-d_{11}, 1.0% octyl β-D-glucoside-d_{24}, and 12.5% D_2O) at pH 8, 6, or 5 was added. The final pH for spectra A, B, and C was 8.1 ± 0.1; for spectra D, E, and F it was 6.3 ± 0.1; and for spectra G, H, and I it was 5.7 ($\pm$0.1). The final concentration of ^{13}C-CMG2 for each spectrum is 6 μM. Spectra A, D, and G correspond to free ^{13}C-CMG2 (unbound) and show virtually superimposable profiles. The final concentration of WT PA_{63} (B, E, and H) and $2FHisPA_{63}$ (C, F, and I) is 3 μM. Note the difference in intensity of ^{13}C-CMG2 at pH 5.7 for WT PA_{63} (spectrum H) and $2FHisPA_{63}$ (spectrum I). Each spectrum represents 2048 transients acquired on an 800 MHz NMR (Bruker, University of Kansas) equipped with a cryoprobe (acquisition time was 1 h for each experiment).

bound to $(2\text{-}FHisPA_{63})_7$ was unchanged, indicating that ^{13}C-CMG2 remained bound. This further supports the SDS–PAGE and potassium release experiments showing that pore formation is largely blocked in the presence of the receptor and suggests that the defect in cytotoxicity associated with 2-FHis labeling is a combination of both a defect in translocation (due to a 2-FH299) and a defect in pore formation, but only when bound to the receptor.

Crystal Structure of 2-FHisPA. These results suggested that the combination of 2-FHis labeling and receptor binding increased the pH stability of the prepore such that low pH-induced pore formation is blocked. Since pore formation of 2-FHis and WT prepore proteins, in the absence of the receptor, could occur at identical pH values (*23*), we reasoned that receptor binding must somehow alter the local environment around the 2-FHis side chains in such a way as to stabilize the structure against changes in pH. Critical to our understanding then was to determine if the local environment (i.e., van der Waals contacts, hydrogen bonding) around the histidine side chains is affected by the presence of fluorine and whether receptor binding changes the environment around the histidine side chains in such a way as to prevent protonation.

Toward understanding whether the environment around the histidine side chains is affected by labeling with fluorine, we have determined, to 1.7 Å resolution, the crystal structure of the full-length, 83 kDa form of 2-FHisPA (Figure 4B). The structure overlays quite well with WT PA (rmsd = 1.118 Å) (*40*), as well as the WT PA-CMG2 complex (rmsd = 0.933 Å) (*22*). The refinement statistics are shown in Table 1. With the exception of 2-FHis-211, -304, and -310 (which are not observed in the crystal structure), all of the 2-FHis residues adopt similar side chain conformations compared to the WT PA and PA–CMG2 structures (Figure 4C), indicating that the presence of fluorine does not significantly perturb the local environment. The histidine side chains are also involved in similar hydrogen-bonding interactions, and because we can visualize the fluorine atom at the 2-position, the N-π and N-τ atoms of the ring can be differentiated (Figure 4A).

Hydrogen Bonding to the Side Chains of 2-FHis. To assess hydrogen bonding to a 2-FHis or His residue, we measured the distances, along with two other parameters, the tilt angle and the planar angle (Figure 5), from either the N-π or N-τ of the imidazole ring to polar atoms ~3 Å away. The tilt angle is similar to the angle between the Fe^{2+} to His F8 in hemoglobin used to distinguish the T to R transition (*41*). The planar angle is the angle measured either above or below the plane of the ring, relative to the center of the ring. A summary of the tilt and planar angles to polar atoms from 2-FHis residues is shown in Table 2, along with measurements taken from the WT PA and PA–CMG2 structures.

It is important to note that the pH values and resolution of the three structures are different (pH 8.2 and 1.7 Å for 2-FHisPA, pH 6 and 2.1 Å for WT PA, and pH ~9 and 2.5 Å for the WT PA–CMG2 complex), and structural changes occur as the pH is lowered; the domain 2 loop connecting strands β3–β4 in WT PA is disordered at low pH (*40*). The values in Table 2 suggest that for most of the 2-FHis residues the hydrogen bonds to the N-π and N-τ atoms are similar to that in either the WT PA or

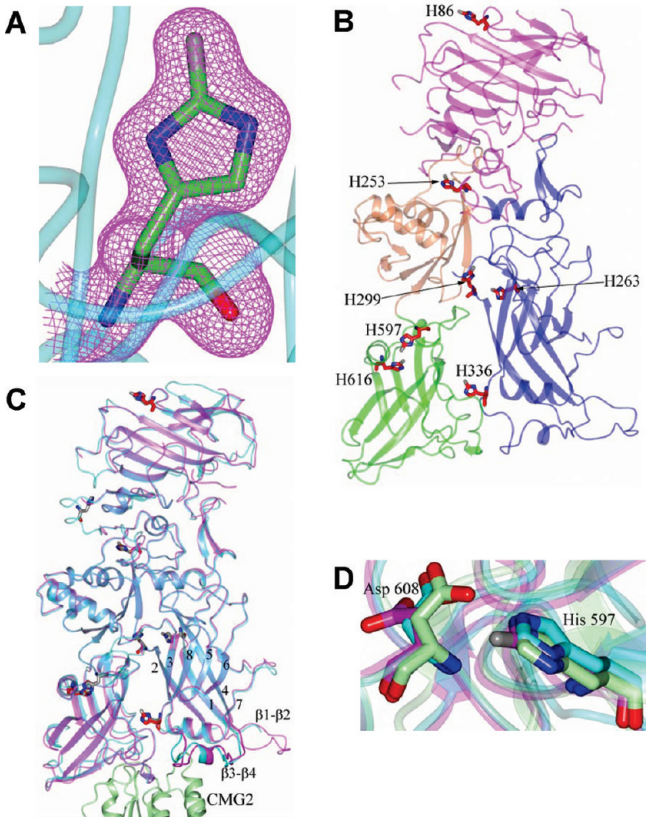

FIGURE 4: (A) $2F_o - F_c$ electron density map of 2-FHis299 contoured at 1σ. (B) Crystal structure of 2-FHisPA (PDB: 3MHZ): domain 1, S15−A258 (magenta); domain 2, Y259−T487 (blue); domain 3, T488−R595 (coral); domain 4, F596−I734 (green). 2-FHis residues are represented as red sticks. (C) Superposition of 2-FHisPA (magenta) and the WT PA (cyan)−CMG2 (green) complex (*22*). The 2-FHis and histidine residues are colored red and gray, respectively. (D) Superposition of H597 and D608 in WT PA (light green), the PA−CMG2 complex (cyan), and 2-FHis597 and D608 in 2-FHisPA (magenta).

PA−CMG2 protein structure. An exception is 2-FH597, which forms a polar interaction with the Oδ1 of D608 in the WT PA and the PA−CMG2 complex, but in the 2-FHisPA structure the D608 side chain is rotated away from 2-FH597 (Figure 4D). In 2-FHisPA, this interaction is replaced with a water molecule. Hydrogen bonding for all observed 2-FHis residues is depicted in Figure 6.

We also note that in the crystal structure of 2-FHisPA we are able to observe the loop connecting strands β1 and β2 (residues D276−R287) and the loop and small helix connecting strands β3 and β4 (residues S339−T357) (Figure 4C). The latter region could be observed in crystal form 1 of WT PA (obtained at pH 7.5) (*40*); however, this structure was never deposited in the PDB, and thus a comparison to our structure was not possible. In that structure, the loop connecting strands β1 and β2 was not observed. We have included the electron density surrounding these loop regions in the Supporting Information (Figure S2). The presence of a crystal contact between R344 and a symmetry-related E224 side chain from another 2-FHisPA molecule likely contributes to the stabilization and observation of the β3−β4 loop (Figure S3, Supporting Information).

Other Noncovalent Contacts to 2-FHis Side Chains. The electronic properties of the C−F bond are quite different from the C−H bond, and the bond length is slightly longer (1.47 Å versus 1.09 Å, respectively). These properties may in some cases

Table 1: Data Collection and Refinement Statistics for 2-FHisPA

	2-FHisPA
data collection	
unit cell parameters (Å)	a = 71.37, b = 93.98, c = 119.12
space group	$P2_12_12_1$
resolution (Å)	50.0−1.70 (1.76−1.70)
wavelength (Å)	1.0000
temperature (K)	100
observed reflections	584535
unique reflections	88352
$\langle I/\sigma(I)\rangle^a$	33.3 (1.9)
completeness (%)^a	98.7 (89.5)
redundancy^a	6.6 (4.7)
R_{sym} (%)^{a,b}	9.3 (58.9)
refinement	
resolution (Å)	50.0−1.7
reflections (working/test)	83119/4400
R_{factor}/R_{free} (%)^c	19.2/22.2
no. of atoms (protein/Ca^{2+}/PEG 400/water)	5307/2/13/400
model quality	
rmsd bond lengths (Å)	0.016
rmsd bond angles (deg)	1.733
average B factor (Å^2)	
all atoms	35.6
protein	35.4
Ca^{2+}	23.6
PEG 400	56.9
water	37.2
coordinate error based on R_{free} (Å)	0.109
Ramachandran plot (chain A/B)	
favored (%)	98.3
allowed (%)	1.7

^{a}Values in parentheses are for the 1.76−1.70 Å resolution shell. $^b R_{sym} = \sum_{hkl}\sum_i|I_i(hkl) - \langle I(hkl)\rangle|/\sum_{hkl}\sum_i I_i(hkl)$, where $I_i(hkl)$ is the intensity measured for the ith reflection and $\langle I(hkl)\rangle$ is the average intensity of all reflections with indices hkl. $^c R_{factor} = \sum_{hkl}||F_o(hkl)| - |F_c(hkl)||/\sum_{hkl}|F_o(hkl)|$; R_{free} is calculated in an identical manner using 5% of randomly selected reflections that were not included in the refinement.

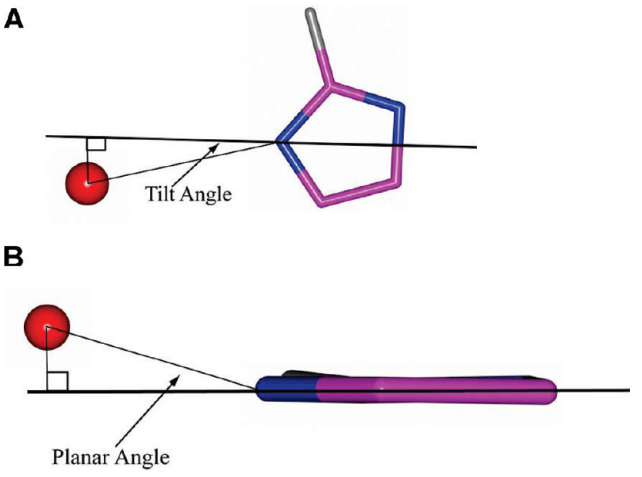

FIGURE 5: Depictions of the tilt and planar angles. The imidazole ring of 2-FHis299 in this example is colored magenta, and a water molecule is represented as a red sphere. (A) The tilt angle is defined as the angular deviation of a particular atom from the plane (bold line) that bisects an N-π or N-τ atom and its opposing N−C bond of the imidazole ring. (B) The planar angle is defined as the angular deviation of a particular atom from the mean plane defined by the imidazole ring atoms (bold line). The distance from the N-π or N-τ to the atom in question is defined as D and its distance from the mean plane as r. The magnitudes of D and r are measurable quantities, and the planar angle can then be calculated by planar angle = $\sin^{-1}(r/D)$.

Table 2: Comparison of Distances, Tilt, and Planar Angles from the N-π, N-τ of Histidine and 2-Fluorohistidine in PA, the PA−CMG2 Complex, and 2-FHisPA

			PA−CMG2[a]			PA[b]			2-FHisPA		
histidine	N-π	N-τ	distance (Å)	tilt angle (deg)	planar angle (deg)	distance (Å)	tilt angle (deg)	planar angle (deg)	distance (Å)	tilt angle (deg)	planar angle (deg)
86	Q121-CO		3.07	31	7.7	3.43	41	22	3.14	26	6.8
253		water				2.90	38	15	2.80	4.0	3.0
253	L255-N		3.05	12	1.5	3.04	1.0	7.6	3.18	5.0	19
263	water		2.70	1.0	10	2.67	11.5	6.0	2.77	3.0	6.0
263		water	2.97	0.3	3.7	2.64	12	7.4	2.78	3.0	4.5
299	water					2.98	32	14	2.75	13	0
299	G323-N		3.0	3.0	32	3.0	7.0	32	3.2	17	20
336		water				2.88	3.0	58	2.79	7.0	3.0
597	E704-Oε1		3.17	4.6	4.3	2.59	0	1.8	2.72	2.0	0.2
597		D608-Oδ1	3.19	10	20	2.82	7.0	3.0			
597		water							2.76	6.0	22
616		Y642-O	2.90	5.0	3.6	2.75	14	6.5	2.80	10	0.2
616	V612-CO		2.75	3.0	17	2.72	8.0	13	2.79	3.0	6.8

[a]See ref *22*. [b]See ref *40*.

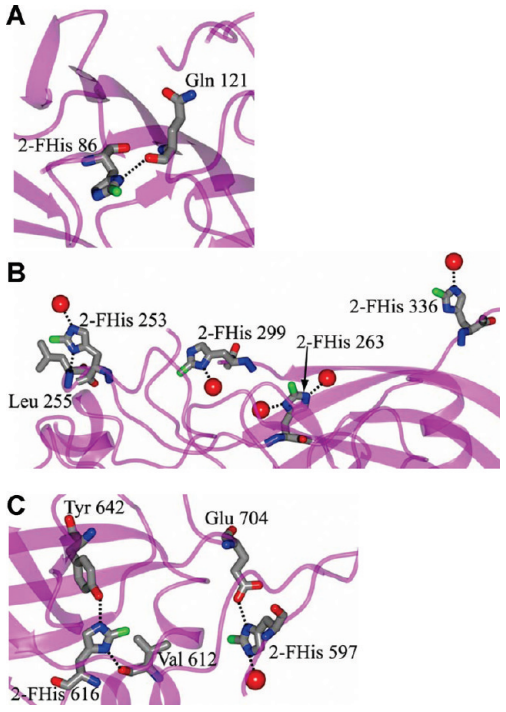

FIGURE 6: Hydrogen bonding of 2-FHis residues in the crystal structure of 2-FHisPA showing residues in individual domains: (A) domain 1, residues S15−A258, (B) 2-FHis253 from domain 1 and domain 2, residues Y259−T487, and (C) domain 4, residues F596−I734. Water molecules are drawn as red spheres.

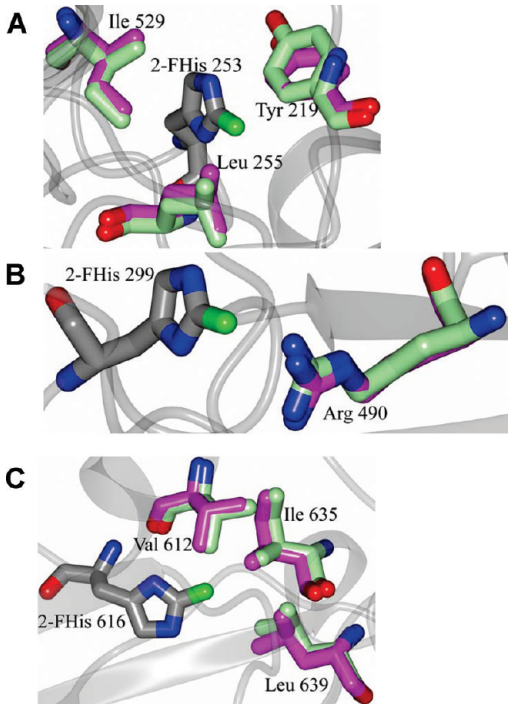

FIGURE 7: Superposition of residues in the WT PA−CMG2 complex (light green) and 2-FHisPA (magenta) near the C−F bond of certain 2-FHis residues: (A) 2-FHis253, (B) 2-FHis299, and (C) 2-FHis616.

strengthen (or weaken) other types of noncovalent interactions with nearby atoms; examples include an effect on molecular packing and van der Waals interactions (*42*), hydrophobicity (*43*, *44*), or dipole interactions (*45*, *46*). For instance, the C−F bond of 2-FH253 is in a hydrophobic patch that is surrounded by Y219, L255, and I529. Similarly, the C−F bond of 2-FH616 is pointing toward a hydrophobic pocket containing V612, I635, and L639. In terms of potential dipole interactions, the C−F bond of 2-FH299 is pointing toward R490, which is within range to form either a C−F···H−N hydrogen bond to the NH2 of the guanidinium (Gdn) or may be involved in a charge−dipole interaction ($C^{\delta+}-F^{\delta-}\cdots Gdn^{+}$). These interactions are represented in Figure 7. Since the side chains of the amino acids surrounding the C−F bonds (hydrophobic or otherwise) have not assumed alternative geometries, this indicates that the C−H to C−F substitutions in PA are isosteric and will likely not affect local structure.

Effect of Receptor Binding on the Rate of H−D Exchange to Histidine Side Chains in PA. Toward understanding whether receptor binding changes the local environment around the histidine side chains, we have monitored the exchange rate of the C_2 imidazole hydrogen of all histidine side chains in WT PA for deuterium by mass spectrometry (*47*, *48*). In this study, both PA alone and the complex with CMG2 were subjected to H−D exchange at pH* 9.5, followed by protease digestion to afford peptides which contained each of the histidines.

Table 3: Histidine-Containing Peptides/Peptide Fragments Monitored To Obtain Rate Constants (k_φ) of H−D Exchange

peptide[a]	amino acid sequence of peptide/peptide fragment	position of peptide/peptide fragment	ions used for calculating the rate of H−D exchange, m/z
H86	ATSADNHVTMW	A90−W100	m/z 616.77 and 617.27 (z = 2)
H211	ISNIHEKKGLTKY	I217−Y229	m/z 383.47 and 383.72 (z = 4)
H253	EKVTGRIDKNVSPEARHPL	E247−L265	m/z 430.04 and 430.24 (z = 5)
H263	HVDMENIILS	H273−S282	m/z 585.80 and 586.30 (z = 2)
H299/304/310 (H299)[b]	THTSE (b_5)	T308−E312	m/z 556.23 and 557.23 (z = 1)
H299/304/310 (H314)	TSEVHGNAEVHA (y_{12}^{2+})	T310−A321	m/z 625.79 and 626.29 (z = 2)
H299/304/310 (H320)	GNAEVHAS (y_7)	G315−A321	m/z 697.33 and 698.33 (z = 1)
H336	SNSNSSTVAIDHSL	S335−L348	m/z 716.34 and 716.84 (z = 2)
H597	HYDRNNIAVGADESVVK	H607−K623	m/z 629.65 and 629.98 (z = 3)
H616	NNIAVGADESVVKEAHR	N611−R627	m/z 603.65 and 603.98 (z = 3)

[a]H211 and H253 peptides were produced by digesting PA with chymotrypsin. The other peptides were produced by digesting the protein using a combination of trypsin and chymotrypsin. [b]H299/304/310 peptide (T308−A321) contains H299, H304, and H310. The amino acid sequences, positions, and monitored ions shown for H299, H304, and H310 are for the fragment ions (b_5, y_{12}^{2+}, and y_7, respectively) produced from the precursor peptide (THTSEVHGNAEVHAS) by collision-induced dissociation.

Table 4: $t_{1/2}$ Values of H−D Exchange at Histidine Residues in PA and the PA−CMG2 Complex

	$t_{1/2}$ (day)	
residue	PA[a]	PA−CMG2
H86	0.80 ± 0.01	0.88 ± 0.05
H211	11.34 ± 0.79	11.45 ± 0.80
H253	> 50	> 50
H263	1.75 ± 0.08	1.84 ± 0.10
H299	**4.41 ± 0.70**	**12.16 ± 0.46**
H304[b]	**2.17 ± 0.50**	**4.78 ± 0.58**
H310	1.68 ± 0.36	1.83 ± 0.01
H336	**8.41 ± 1.50**	**31.72 ± 5.57**
H597	0.66 ± 0.01	0.69 ± 0.02
H616	> 50	> 50

[a]Data are means ± standard deviation from triplicate reactions. See Table 3 for the amino acid sequences of peptides/peptide fragments used to determine the k_φ. [b]The $t_{1/2}$ values were determined indirectly by subtracting the rate constant (k_φ) of H−D exchange for His310 from the combined k_φ for His304 and His310.

The resulting peptides were analyzed by LC-MS/MS. All ten histidine residues were detected in eight different peptides (Table 3). Initially, the peptides were assigned to the amino acid sequence of PA by matching the experimentally obtained peptide masses to their expected molecular masses. The tandem mass spectra for these peptides ensured that the assignments were correct (Figure S4a−h, Supporting Information). Peptide ions used for calculating the rate constants (k_φ) of H−D exchange at each of the histidine residue are also shown in Table 3. The $t_{1/2}$ values of H−D exchange at each of the histidines, both in the presence and absence of CMG2, are shown in Table 4.

First, the data show that the $t_{1/2}$ values are consistent with the degree of solvent exposure of each of the side chains seen in the crystal structure. For instance, both H83 and H597, which have short $t_{1/2}$ values (less than 1 day), are solvent exposed; H253 and H616 have very long half-lives: H253 is in a region which has low temperature factors, and H616 is buried within the core of domain 4 (see Figure 7). In the presence of the receptor, the most dramatic changes in the $t_{1/2}$ values are centered within domain 2 and include H299, H336 (exchange rates ~3-fold slower), and H304 (~2-fold slower rate). This indicates that receptor binding either stabilizes hydrogen-bonding interactions to these histidine residues or decreases the ability of these histidines to exchange protons with solvent. With the exception of H336, which lies at the interface between domain 2 and domain 4 (Figure 4), and H304 (which is not observed in the crystal structure), H299 is > 40 Å from the binding interface.

DISCUSSION

The role of histidine in governing the conformational change from a soluble prepore to a membrane spanning pore was first investigated in a previous study by labeling PA with 2-FHis, an isosteric analogue of histidine with a side-chain pK_a of ~1 (*23*). In that study, we showed that 2-FHisPA is defective in mediating cytotoxicity of CHO-K1 cells by LF_N−DTA, and here we demonstrate that this defect is likely due to a combination of two separate processes: an inability to translocate derivatives of LF and an inability to form a membrane spanning pore when bound to the vWA domain of CMG2.

The defect in translocation associated with 2-FHis labeling is shown to be due primarily to 2-FH299, which, based on previous biochemical experiments, is projected to be on the outside of the pore in contact with the solvent (*13*, *14*). It may be that labeling H299 with 2-FHis causes a deformation of the pore structure that prevents translocation, an effect that does not occur upon mutation of H299 to glutamine. In any case, the ability of the 2-FH299Q mutant to translocate LF_N suggests that histidine protonation is not directly involved in the process of protein translocation.

Despite the ability to translocate LF_N, the 2-FH299Q mutant was incapable of mediating LF_N−DTA cytotoxicity of CHO-K1 cells. Using a combination of SDS−PAGE, potassium release experiments, and HSQC-NMR, we show that pore formation of the 2-FHis-labeled $(PA_{63})_7$ is, to a large extent, blocked in the presence of the vWA domain of CMG2. We use the term "large extent" to note that the block we observe in the SDS−PAGE assay and potassium release assay is not complete; as mentioned, we are able to observe faint bands at pH 5 and 6 in the SDS−PAGE assay and a small increase in potassium release. This may indicate that there is a small amount of unlabeled, WT PA in our preparation or that the mechanism of pore formation is heterogeneous. In the latter case, there may be some fraction of 2-FHis-labeled molecules that, upon binding to the receptor, is in a conformation where pore formation occurs at pH values similar to the WT protein. However, for the majority of molecules we observe, the combination of 2-FHis labeling and receptor binding is sufficient to block low pH-induced pore formation.

Pore formation is known to involve the peeling of domain 2 strands β2 and β3 from domain 2, since residues from these two strands largely comprise the 70 Å long pore (*13*, *14*). However, the crystal structure of WT PA or prepore bound to CMG2 (*22*, *35*) revealed that, while the receptor binds primarily to domain 4, the receptor also interacts with a loop connecting the domain 2 strands β3 and β4 (Figure 4C). This loop was hypothesized to be important for enhancing the stability of the prepore to pH (*22*). For instance, the pH threshold for pore formation is reduced from a pH of ~7 in the absence of the receptor to ~6 when bound to TEM8 and ~5 when bound to CMG2 (*36*, *37*). Residues in CMG2 which form hydrogen bonds with the domain 2 β3−β4 loop have been shown to be important for the enhanced pH stability of the prepore (*36*, *49*, *50*). Mechanistically, binding of the receptor stabilizes the domain 2 β3−β4 loop, which stabilizes domain 2 against pH-dependent changes.

The addition of the receptor to WT PA also reduces the rate of H−D exchange of the C_2 imidazole hydrogen of histidine residues 304, 299, and 336 within domain 2 (Table 4). Therefore, the stabilizing influence of receptor binding is not only localized to the domain 2 β3−β4 loop but is propagated to sites distant from the binding interface. Based on the crystal structures of PA and PA bound to CMG2, the environments around the histidine side chains are virtually identical, suggesting that the slower rate of H−D exchange is unlikely to be due to a decrease in solvent exposure. Unfortunately, we could not confirm that the pK_a of the histidine side chains decreases upon binding the receptor, which may occur if the hydrogen bonds to the histidine imidazole (acting as a proton acceptor) are strengthened. Further, we could not confirm that the rate of H−D exchange is also slowed upon binding the receptor to 2-FHisPA using the C_2 exchange strategy. H−D exchange at the C_2 of histidine proceeds through the abstraction of the C_2 proton from the cationic imidazolium (both nitrogens protonated) by OD^-, to form an ylide or a carbene intermediate, which is the rate-determining step in the reaction (*47*). An analogous exchange with 2-FHis cannot be observed because this would require formal removal of F^+, an energetically impossible event.

The stability to pH of 2-FHisPA is greater than WT PA (pK_{app} of 3.6 vs 5.9 for WT PA) (*23*). Despite the observed increase in pH stability, the prepore form undergoes pore formation at nearly identical pH values as the WT (*23*). This would indicate that the pH stabilizing influence of 2-FHis is lost upon conversion to the prepore. But, in the presence of the receptor, pH-dependent pore formation from the $(2\text{-FHisPA}_{63})_7$ prepore is, to a large extent, blocked. This would indicate that receptor binding restores the pH stability observed in the full-length, monomeric 2-FHisPA. The H−D exchange experiments also indicate that histidine protonation, required for the process of H−D exchange in our strategy, is slowed for WT PA in the presence of the receptor. Together with the crystal structure of 2-FHisPA and the comparison of hydrogen-bonding patterns to the WT and PA-CMG2 structures, our combined results indicate that receptor binding prevents protonation of histidine residues, which subsequently blocks low-pH induced pore formation.

To explain how receptor binding may influence protonation, we propose a model in which the prepore structure is rather dynamic and "floppy"; binding of the receptor to the prepore decreases this motion, resulting in the strengthening of hydrogen-bonding interactions and an overall tightening of the structure. The model of positive cooperativity put forth by Williams would indicate that binding of the receptor results in an overall tightening of the structure which experiences, in the absence of receptor, extensive molecular motion (*51*, *52*). In a system similar to ours, calorimetric analysis of the binding of the receptor ganglioside GM1 to diphtheria toxin was shown to exhibit positive cooperativity (*53*). Evidence from experiments monitoring pore formation as a function of pH has already shown that receptor binding to the WT PA prepore leads to an increase in the degree of cooperative interactions; while the pH stability is enhanced, the slope of the transition from a prepore to a pore is much steeper and occurs over a narrower pH range (*35*, *37*). Binding of the receptor may decrease the global molecular motion of the prepore, facilitating an increase in hydrogen-bonding interactions and thereby eliciting a similar positive cooperative effect.

Since all of the 2-FHis residues will have a lower pK_a compared to their histidine counterparts, those histidines in which protonation disrupts hydrogen bonding will likely remain unprotonated at pH 5, such that the hydrogen bonds to the 2-FHis imidazole ring (which may be strengthened by receptor binding) are maintained. Because of the electron-withdrawing inductive effect of the fluorine, the 2-FHis imidazole nitrogens are expected to be relatively weak hydrogen bond acceptors, due to less basicity of the imidazole nitrogens, but better hydrogen bond donors. Since we cannot assign to which nitrogen the hydrogen is bound, it is difficult to determine which of the two nitrogens is participating as a hydrogen bond donor or acceptor. We can surmise, for instance, that the NH of L255 is participating as a hydrogen bond donor to the π nitrogen of H253; similarly, the NH of G253 likely donates a hydrogen bond to the π nitrogen of H299 (Table 1). Protonation of the π nitrogen at these, or other, sites would be expected to disrupt hydrogen bonding. However, labeling with 2-FHis may prevent protonation, such that these hydrogen bonds are maintained.

Although all of the 2-FHis residues that we could observe are involved in hydrogen-bonding interactions, we cannot rule out that other types of noncovalent interactions are also influenced by 2-FHis labeling, including electrostatic/dipole or hydrophobic interactions (Figure 7) (*42*−*46*). Since the side chains of the amino acids surrounding the C−F bonds have not assumed alternative geometries or packing from that of the WT protein, this suggests that the C−F bond may exhibit only minor changes in local interaction energies. Nonetheless, a "polar-hydrophobic" effect might increase stability without leading to altered geometries. Thus, as discussed by DiMagno and co-workers, the C−F bond is polarized, and in an aqueous environment, water molecules are aligned with the C−F dipole. When the C−F bond enters a hydrophobic pocket, these water molecules are shed, leading to an increase in entropy and an increase in stability (*46*).

Given that we know so little about the effect of fluorine on the electronic properties of 2-FHis, but do know that 2-FHis has a lower pK_a and thus is more difficult to protonate at physiologic pH, our combined results are most consistent with an effect on protonation. This conclusion is also consistent with studies in which RNase A was chemically synthesized to contain 4-fluorohistidine (4-FHis), another analogue of histidine with a side-chain pK_a of 3.5. The pH−rate profiles observed were consistent with a lower pK_a of 4-FHis, lowering the pH required for catalysis, without an effect on enzyme structure (*54*).

In conclusion, our study suggests that protonation of histidine residues, in particular those in domain 2, contributes to the mechanism of pore formation but only when bound to the receptor. Further, our study suggests that there are at least two

separate mechanisms for pore formation: one in which the receptor is unbound and histidine protonation is unimportant, and another in which the receptor is bound and histidine protonation becomes a part of the mechanism for pore formation. Understanding how these mechanisms may cooperate in controlling pH-dependent pore formation will certainly contribute to a better understanding of anthrax disease pathogenesis.

ACKNOWLEDGMENT

We are grateful for the support of Dr. R. John Collier, whose laboratory is supported by NIH R01 AI022021, which provided financial support to B.E.J. and J.S.

SUPPORTING INFORMATION AVAILABLE

Figures of translocation of LF_N-DTA, a simulated-annealing omit map for the $\beta1-\beta2$ and $\beta3-\beta4$ loops, a figure showing the crystal contact between R344 and E224, and mass spectra of peptides used in the H−D exchange experiments. This material is available free of charge via the Internet at http://pubs.acs.org.

REFERENCES

1. Young, J. A., and Collier, R. J. (2007) Anthrax toxin: receptor binding, internalization, pore formation, and translocation. *Annu. Rev. Biochem. 76*, 243–265.
2. Bradley, K. A., Mogridge, J., Mourez, M., Collier, R. J., and Young, J. A. (2001) Identification of the cellular receptor for anthrax toxin. *Nature 414*, 225–229.
3. Scobie, H. M., Rainey, G. J., Bradley, K. A., and Young, J. A. (2003) Human capillary morphogenesis protein 2 functions as an anthrax toxin receptor. *Proc. Natl. Acad. Sci. U.S.A. 100*, 5170–5174.
4. Klimpel, K. R., Molloy, S. S., Thomas, G., and Leppla, S. H. (1992) Anthrax toxin protective antigen is activated by a cell surface protease with the sequence specificity and catalytic properties of furin. *Proc. Natl. Acad. Sci. U.S.A. 89*, 10277–10281.
5. Milne, J. C., Furlong, D., Hanna, P. C., Wall, J. S., and Collier, R. J. (1994) Anthrax protective antigen forms oligomers during intoxication of mammalian cells. *J. Biol. Chem. 269*, 20607–20612.
6. Melnyk, R. A., Hewitt, K. M., Lacy, D. B., Lin, H. C., Gessner, C. R., Li, S., Woods, V. L., Jr., and Collier, R. J. (2006) Structural determinants for the binding of anthrax lethal factor to oligomeric protective antigen. *J. Biol. Chem. 281*, 1630–1635.
7. Kintzer, A. F., Thoren, K. L., Sterling, H. J., Dong, K. C., Feld, G. K., Tang II, Zhang, T. T., Williams, E. R., Berger, J. M., and Krantz, B. A. (2009) The protective antigen component of anthrax toxin forms functional octameric complexes. *J. Mol. Biol. 392*, 614–629.
8. Beauregard, K. E., Collier, R. J., and Swanson, J. A. (2000) Proteolytic activation of receptor-bound anthrax protective antigen on macrophages promotes its internalization. *Cell Microbiol. 2*, 251–258.
9. Abrami, L., Liu, S., Cosson, P., Leppla, S. H., and van der Goot, F. G. (2003) Anthrax toxin triggers endocytosis of its receptor via a lipid raft-mediated clathrin-dependent process. *J. Cell Biol. 160*, 321–328.
10. Abrami, L., Lindsay, M., Parton, R. G., Leppla, S. H., and van der Goot, F. G. (2004) Membrane insertion of anthrax protective antigen and cytoplasmic delivery of lethal factor occur at different stages of the endocytic pathway. *J. Cell Biol. 166*, 645–651.
11. Miller, C. J., Elliott, J. L., and Collier, R. J. (1999) Anthrax protective antigen: prepore-to-pore conversion. *Biochemistry 38*, 10432–10441.
12. Katayama, H., Janowiak, B. E., Brzozowski, M., Juryck, J., Falke, S., Gogol, E. P., Collier, R. J., and Fisher, M. T. (2008) GroEL as a molecular scaffold for structural analysis of the anthrax toxin pore. *Nat. Struct. Mol. Biol. 15*, 754–760.
13. Benson, E. L., Huynh, P. D., Finkelstein, A., and Collier, R. J. (1998) Identification of residues lining the anthrax protective antigen channel. *Biochemistry 37*, 3941–3948.
14. Nassi, S., Collier, R. J., and Finkelstein, A. (2002) PA63 channel of anthrax toxin: an extended beta-barrel. *Biochemistry 41*, 1445–1450.
15. Krantz, B. A., Finkelstein, A., and Collier, R. J. (2006) Protein translocation through the anthrax toxin transmembrane pore is driven by a proton gradient. *J. Mol. Biol. 355*, 968–979.
16. Krantz, B. A., Trivedi, A. D., Cunningham, K., Christensen, K. A., and Collier, R. J. (2004) Acid-induced unfolding of the amino-terminal domains of the lethal and edema factors of anthrax toxin. *J. Mol. Biol. 344*, 739–756.
17. Tang, W. J., and Guo, Q. (2009) The adenylyl cyclase activity of anthrax edema factor. *Mol. Aspects Med. 30*, 423–430.
18. Lehmann, M., Noack, D., Wood, M., Perego, M., and Knaus, U. G. (2009) Lung epithelial injury by *B. anthracis* lethal toxin is caused by MKK-dependent loss of cytoskeletal integrity. *PLoS ONE 4*, e4755.
19. Krantz, B. A., Melnyk, R. A., Zhang, S., Juris, S. J., Lacy, D. B., Wu, Z., Finkelstein, A., and Collier, R. J. (2005) A phenylalanine clamp catalyzes protein translocation through the anthrax toxin pore. *Science 309*, 777–781.
20. Thoren, K. L., Worden, E. J., Yassif, J. M., and Krantz, B. A. (2009) Lethal factor unfolding is the most force-dependent step of anthrax toxin translocation. *Proc. Natl. Acad. Sci. U.S.A. 106*, 21555–21560.
21. Blaustein, R. O., Koehler, T. M., Collier, R. J., and Finkelstein, A. (1989) Anthrax toxin: channel-forming activity of protective antigen in planar phospholipid bilayers. *Proc. Natl. Acad. Sci. U.S.A. 86*, 2209–2213.
22. Santelli, E., Bankston, L. A., Leppla, S. H., and Liddington, R. C. (2004) Crystal structure of a complex between anthrax toxin and its host cell receptor. *Nature 430*, 905–908.
23. Wimalasena, D. S., Cramer, J. C., Janowiak, B. E., Juris, S. J., Melnyk, R. A., Anderson, D. E., Kirk, K. L., Collier, R. J., and Bann, J. G. (2007) Effect of 2-fluorohistidine labeling of the anthrax protective antigen on stability, pore formation, and translocation. *Biochemistry 46*, 14928–14936.
24. Eichler, J. F., Cramer, J. C., Kirk, K. L., and Bann, J. G. (2005) Biosynthetic incorporation of fluorohistidine into proteins in *E. coli*: a new probe of macromolecular structure. *ChemBioChem 6*, 2170–2173.
25. Kirk, K. L., Nagai, W., and Cohen, L. A. (1973) Photochemistry of diazonium salts. II. Synthesis of 2-fluoro-L-histidine and 2-fluorohistamine, and the halogen lability of 2-fluoroimidazoles. *J. Am. Chem. Soc. 95*, 8389–8392.
26. Rajapaksha, M., Eichler, J. F., Hajduch, J., Anderson, D. E., Kirk, K. L., and Bann, J. G. (2009) Monitoring anthrax toxin receptor dissociation from the protective antigen by NMR. *Protein Sci. 18*, 17–23.
27. Sun, J., Lang, A. E., Aktories, K., and Collier, R. J. (2008) Phenylalanine-427 of anthrax protective antigen functions in both pore formation and protein translocation. *Proc. Natl. Acad. Sci. U.S.A. 105*, 4346–4351.
28. Janowiak, B. E., Finkelstein, A., and Collier, R. J. (2009) An approach to characterizing single-subunit mutations in multimeric prepores and pores of anthrax protective antigen. *Protein Sci. 18*, 348–358.
29. Sun, J., Vernier, G., Wigelsworth, D. J., and Collier, R. J. (2007) Insertion of anthrax protective antigen into liposomal membranes: effects of a receptor. *J. Biol. Chem. 282*, 1059–1065.
30. Otwinowski, Z., and Minor, W. (1997) Processing of X-ray diffraction data collected in oscillation mode, in Methods in Enzymology, Macromolecular Crystallography, Part A (Carter, C. W., and Sweet, R. M., Eds.) pp 307−326, Academic Press, New York.
31. Murshudov, G. N., Vagin, A. A., and Dodson, E. J. (1997) Refinement of macromolecular structures by the maximum-likelihood method. *Acta Crystallogr., Sect. D: Biol. Crystallogr. 53*, 240–255.
32. Painter, J., and Merritt, E. A. (2006) TLSMD web server for the generation of multi-group TLS models. *J. Appl. Crystallogr. 39*, 109–111.
33. Emsley, P., and Cowtan, K. (2004) Coot: model-building tools for molecular graphics. *Acta Crystallogr., Sect. D: Biol. Crystallogr. 60*, 2126–2132.
34. Lovell, S. C., Davis, I. W., Arendall, W. B., 3rd, de Bakker, P. I., Word, J. M., Prisant, M. G., Richardson, J. S., and Richardson, D. C. (2003) Structure validation by Calpha geometry: phi,psi and Cbeta deviation. *Proteins 50*, 437–450.
35. Lacy, D. B., Wigelsworth, D. J., Melnyk, R. A., Harrison, S. C., and Collier, R. J. (2004) Structure of heptameric protective antigen bound to an anthrax toxin receptor: a role for receptor in pH-dependent pore formation. *Proc. Natl. Acad. Sci. U.S.A. 101*, 13147–13151.
36. Scobie, H. M., Marlett, J. M., Rainey, G. J., Lacy, D. B., Collier, R. J., and Young, J. A. (2007) Anthrax toxin receptor 2 determinants that dictate the pH threshold of toxin pore formation. *PLoS ONE 2*, e329.
37. Rainey, G. J., Wigelsworth, D. J., Ryan, P. L., Scobie, H. M., Collier, R. J., and Young, J. A. (2005) Receptor-specific requirements for anthrax toxin delivery into cells. *Proc. Natl. Acad. Sci. U.S.A. 102*, 13278–13283.
38. Wigelsworth, D. J., Krantz, B. A., Christensen, K. A., Lacy, D. B., Juris, S. J., and Collier, R. J. (2004) Binding stoichiometry and

kinetics of the interaction of a human anthrax toxin receptor, CMG2, with protective antigen. *J. Biol. Chem. 279*, 23349–23356.
39. Arac, D., Murphy, T., and Rizo, J. (2003) Facile detection of protein-protein interactions by one-dimensional NMR spectroscopy. *Biochemistry 42*, 2774–2780.
40. Petosa, C., Collier, R. J., Klimpel, K. R., Leppla, S. H., and Liddington, R. C. (1997) Crystal structure of the anthrax toxin protective antigen. *Nature 385*, 833–838.
41. Perutz, M. F. (1970) Stereochemistry of cooperative effects in haemoglobin. *Nature 228*, 726–739.
42. Minks, C., Huber, R., Moroder, L., and Budisa, N. (1999) Atomic mutations at the single tryptophan residue of human recombinant annexin V: effects on structure, stability, and activity. *Biochemistry 38*, 10649–10659.
43. Bilgicer, B., Fichera, A., and Kumar, K. (2001) A coiled coil with a fluorous core. *J. Am. Chem. Soc. 123*, 4393–4399.
44. Son, S., Tanrikulu, I. C., and Tirrell, D. A. (2006) Stabilization of bzip peptides through incorporation of fluorinated aliphatic residues. *ChemBioChem 7*, 1251–1257.
45. O'Hagan, D. (2008) Understanding organofluorine chemistry. An introduction to the C-F bond. *Chem. Soc. Rev. 37*, 308–319.
46. Biffinger, J. C., Kim, H. W., and DiMagno, S. G. (2004) The polar hydrophobicity of fluorinated compounds. *ChemBioChem 5*, 622–627.
47. Miyagi, M., and Nakazawa, T. (2008) Determination of pK_a values of individual histidine residues in proteins using mass spectrometry. *Anal. Chem. 80*, 6481–6487.
48. Takeuchi, Y. Y., Herman, J. C., Kirk, K. L., and Cohen, L. A. (1978) Adjacent lone pair (ALP) effects in heteroaromatic systems. 1. Isotope exchange of ring hydrogens in alkylimidazoles. *J. Org. Chem. 43*, 3565–3570.
49. Liu, S., Leung, H. J., and Leppla, S. H. (2007) Characterization of the interaction between anthrax toxin and its cellular receptors. *Cell Microbiol. 9*, 977–987.
50. Gao, M., and Schulten, K. (2006) Onset of anthrax toxin pore formation. *Biophys. J. 90*, 3267–3279.
51. Williams, D. H., Maguire, A. J., Tsuzuki, W., and Westwell, M. S. (1998) An analysis of the origins of a cooperative binding energy of dimerization. *Science 280*, 711–714.
52. Williams, D. H., Stephens, E., O'Brien, D. P., and Zhou, M. (2004) Understanding noncovalent interactions: ligand binding energy and catalytic efficiency from ligand-induced reductions in motion within receptors and enzymes. *Angew. Chem., Int. Ed. Engl. 43*, 6596–6616.
53. Schon, A., and Freire, E. (1989) Thermodynamics of intersubunit interactions in cholera toxin upon binding to the oligosaccharide portion of its cell surface receptor, ganglioside GM1. *Biochemistry 28*, 5019–5024.55.
54. Jackson, D. Y., Burnier, J., Quan, C., Stanley, M., Tom, J., and Wells, J. A. (1994) A designed peptide ligase for total synthesis of ribonuclease A with unnatural catalytic residues. *Science 266*, 243–247.